JOURNAL OF MATERIALS SCIENCE **38** (2003) 3629–3639

# Analysis of the diametrical compression test and the applicability to plastically deforming materials

A. T. PROCOPIO
*Merck Research Laboratories, West Point, PA 19486, USA*
*E-mail: adam_procopio@merck.com*

A. ZAVALIANGOS
*Drexel University, Philadelphia, PA 19104, USA*

J. C. CUNNINGHAM
*Merck Research Laboratories, West Point, PA 19486, USA*

The effect of contact flattening and material properties on the fracture stress calculation for the diametrical compression test used to evaluate compact strength was examined through finite element simulations. Two-dimensional simulations were carried out using linear elastic, elastoplastic, and porous elastoplastic models with commercial finite element software. A parametric study was performed by varying the elastic modulus ($E$), Poisson's ratio ($\nu$), contact frictional coefficient ($\mu$), yield stress ($\sigma_{\text{yield}}$), and compact relative density (RD). Stress contours generated from these simulations were compared to the Hertzian and Hondros analytical expressions. Linear elastic simulations show excellent agreement with the analytical solutions. Significant deviation, however, occurs for the elastoplastic and porous elastoplastic simulations at larger diametrical strain with material plasticity. A better understanding of the stress-state of diametrically loaded plastically deforming disks has been demonstrated in this computational and experimental work. Results from these finite element simulations confirm that the standard tensile strength calculation: $\sigma_{\text{f}} = 2P/\pi Dt$, is suitable for linear elastic materials. However, the incorporation of plasticity into the material model results in a significant change in the maximum principal stress field (magnitude and location) rendering the Hertzian estimate of tensile strength invalid. A map to check the validity of the Hertzian equation is proposed. 

## 1. Introduction

A fracture criterion is typically expressed as the relationship between an externally applied stress field, the geometry of defects in a specimen, and material properties (namely fracture toughness). Such fracture criteria can be used in conjunction with an experiment [1–3] to determine the fracture toughness of a material, if defect geometry and external stresses are known, or to estimate the maximum size of defects present in a component if fracture toughness and external stresses are known.

Strength tests such as the tension test, the diametrical compression test, and the simple compression test determine the limit of performance of a material to stress. As such, strength criteria can be built using a combination of the local principal stresses. For brittle materials, these limiting stress-states (Fig. 1) reflect the *combination* of the fracture toughness of the material and the presence of defects in the tested specimen. Such tests are applicable when we are interested in characterizing the fracture related mechanical performance of specimens in which exact knowledge of the defects and their interaction with the local stress is unknown. Ideally, these tests require: (a) uniform defect population, otherwise the local stress-state is unknown, (b) specified fixed stress mode, (c) consideration of statistical volume-based Weibull-type arguments, which take into account the probability of the presence of defects with critical sizes over the volume of the specimen [2–6].

The diametrical compression test is also known as: the diametrical tensile test, Brazilian disk test, indirect tensile test, compact crushing test, or compact hardness test. It is used as a mechanical testing technique spanning many technological fields, from concrete [7–9] to ceramics [10–13] to metal composites [14, 15] to materials used in dentistry [16–18], to materials used in the processing of pharmaceutical dosage forms [2, 3, 19–23]. The test induces a local tensile stress in the transverse direction of the applied compressive stress. The diametrical compressive test allows for the use of simple specimen geometry (disk, compact, tablet, etc.) to measure a limit force required to cause failure, which is used in the estimation of tensile strength (Equation 4). The simple geometry and loading conditions are attractive for materials which are too difficult to process or machine into the ASTM standard "dogbone" shaped specimen [1], which is pulled in tension, or the more

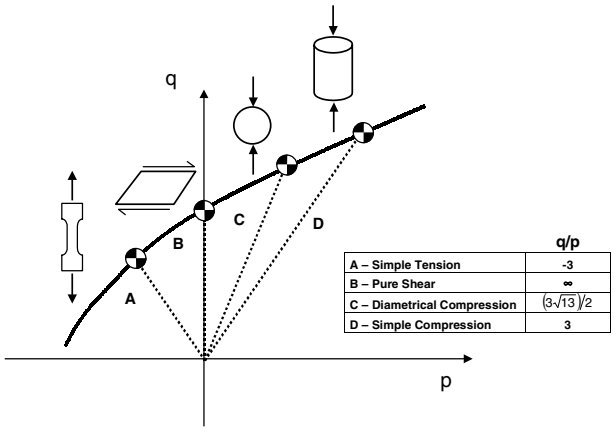


*Figure 1* Schematic representation of a failure locus near the shear stress dominant region for pressure-dependent yielding materials. $p = 1/3\,(\sigma_x+\sigma_y+\sigma_z)$ hydrostatic (compressive) stress; $q = \{(1/2)[(\sigma_x-\sigma_y)^2+(\sigma_y-\sigma_z)^2+(\sigma_x-\sigma_z)^2]\}^{1/2}$ Mises equivalent shear stress; where $\sigma_x$, $\sigma_y$, and $\sigma_z$ represent the principal directions of stress.

appropriate fracture toughness compact tension sample [24].

In the diametrical compression test, we assume that the tensile strength of the specimen can be expressed in terms of the maximum principal tensile stress in the sample. The practical usage of this test often violates all or most of the three conditions stated above. Distribution of the defects is often non-uniform, the stress mode may vary, and statistical arguments are not used because despite their rigor, they are cumbersome to handle. Despite these disadvantages, simple geometry, ease of specimen preparation, and quickness of testing, in addition to empirical correlations with other aspects of mechanical behavior (e.g., simple compact tension [25]), have rendered the diametrical compression test popular in industry. Analogous to the diametrical compression test, is the Charpy impact test used with metallic materials of various ductility, and the melt flow index for polymer processing, which despite the fact they are not "clean" fundamental tests, are very useful in industry. It is often argued that such tests provide useful information within a group of similar materials with a small composition/structure variation or for a given material within a relatively narrow processing parameter window. In any case, the usefulness of the results relies heavily on the ability of the engineer to understand the details of the test in order to identify the applicability window.

The diametrical compression test has been used to estimate strength for elastically deforming materials, which are susceptible to brittle fracture. Because of the ease of testing and the simple specimen geometry, this test is often applied to materials which exhibit limited but measurable macroscopic plastic deformation before fracture [10, 14, 15, 21, 23, 26–28]. It is often claimed that the test in that case is invalid. Given that the test is used in industry, it is important to understand the implications of limited ductility on this test. To this end, in this work, we focus our effort in offering a better understanding of the diametrical stress-state in specimens with some level of permanent deformation before fracture, through numerical analysis and experiments.

## 2. Background

In 1895, Hertz [29] had developed mathematical expressions (Equations 1–3) to describe the stress-states for elastic disks and spheres under diametrical compression under point loading conditions (Fig. 2a).

$$\sigma_x = \frac{-2P}{\pi t}\left\{\frac{x^2(R-y)}{\beta_1^4}+\frac{x^2(R+y)}{\beta_2^4}-\frac{1}{2R}\right\} \quad (1)$$

$$\sigma_y = \frac{-2P}{\pi t}\left\{\frac{(R-y)^3}{\beta_1^4}+\frac{(R+y)^3}{\beta_2^4}-\frac{1}{2R}\right\} \quad (2)$$

$$\sigma_{xy} = \frac{2P}{\pi t}\left\{\frac{x(R-y)^2}{\beta_1^4}+\frac{x(R+y)^2}{\beta_2^4}\right\} \quad (3)$$

$\beta_1^2 = (R-y)^2+x^2$, $\beta_2^2 = (R+y)^2+x^2$, $P$ is the load to fracture, $R$ is the radius, and $t$ is the thickness.

The Hertz solution predicts that the maximum principal stress occurs in the center of the disk, and is tensile along the $x$-direction. Assuming that the maximum tensile principal stress is responsible for the failure of the specimen, the tensile strength, $\sigma_f$, is obtained by

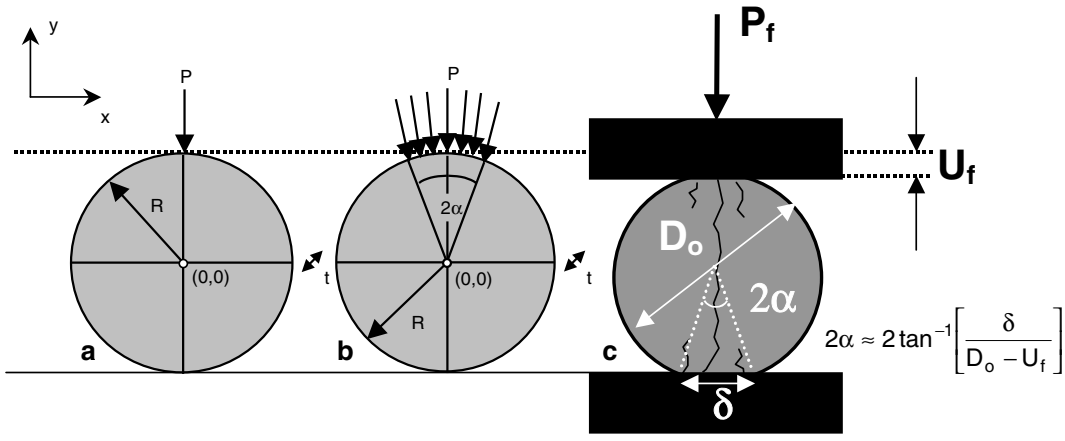


*Figure 2* Schematic representation (a) Hertz point loading conditions, (b) Hondros distributed loading conditions, and (c) uni-axial diametrical compression (top platen compressing) and cracks present after failure along with major measurable variables: $P_f$ = failure load; $U_f$ = displacement at failure; $D_0$ = initial diameter; $\delta$ = contact flattened width; $2\alpha$ = contact flattened angle.

substituting $x = y = 0$ in Equation 1:

$$\sigma_f = \frac{2P}{\pi Dt} \tag{4}$$

where $D$ is the diameter.

The work of Hertz was later modified by Hondros [7] to include distributed loading conditions (Fig. 2b). The Hondros solution along $x = 0$ and $y = 0$ respectively is given by:

$$\sigma_{\theta y}, \sigma_{\theta x} = \pm\frac{2P}{\alpha\pi Dt}\left[\frac{(1 - r^2/R^2)\sin 2\alpha}{(1 \mp 2r^2/R^2\cos 2\alpha + r^4/R^4)} \mp \tan^{-1}\left(\frac{1 \pm r^2/R^2}{1 \mp r^2/R^2}\tan\alpha\right)\right] \tag{5}$$

$$\sigma_{ry}, \sigma_{rx} = \mp\frac{2P}{\alpha\pi Dt}\left[\frac{(1 - r^2/R^2)\sin 2\alpha}{(1 \mp 2r^2/R^2\cos 2\alpha + r^4/R^4)} \pm \tan^{-1}\left(\frac{1 \pm r^2/R^2}{1 \mp r^2/R^2}\tan\alpha\right)\right] \tag{6}$$

$$\tau_{r\theta} = 0 \tag{7}$$

Mathematically, both analyses are exact elasticity solutions and satisfy equations of equilibrium. The analysis by Hertz [29–31] and Hondros [7] converge to Equation 4 at $x = y = 0$ for $2\alpha \to 0$. The solutions assume the following: (i) small strains are involved, (ii) frictionless contact at the boundary, (iii) point loading conditions for the Hertz equations, and (iv) distributed loading conditions over an arc for the Hondros equations. There has been a significant amount of work [11, 17, 26, 32, 33] related to the Hondros distributed loading conditions, numerically and through the use of experimental techniques, such as padding materials on the platens [11, 17] or grinding of the contact face [32]. Experimentally, the effect of load conditions on failure and stress distribution has been shown to be significant through computational techniques [26, 32, 33], the use of controlled platen geometry (both size [22] and shape [16, 17]) and platen material properties [11] as well as ground specimen contacts [32]. Hondros' solution

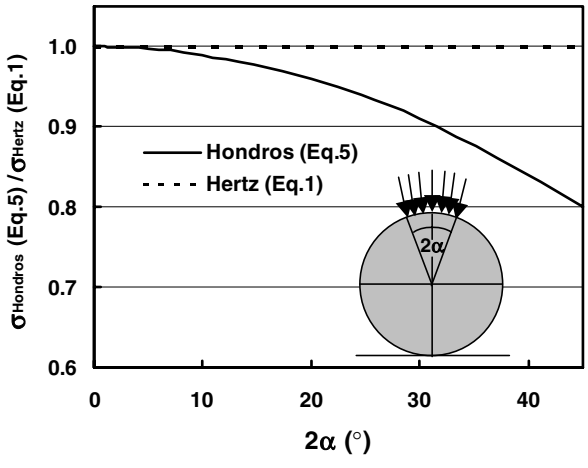


*Figure 3* Normalized tensile stress based on Hondros distributed loading conditions as a function of distributed loading angle, $2\alpha$ [7].

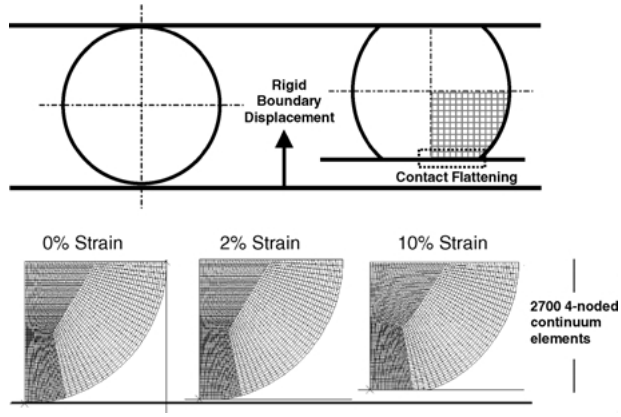


*Figure 4* Representation of the finite element mesh used to simulate diametrical compression. Advantage is taken of the geometric symmetry.

shows (Fig. 3) that a distributed load will affect the maximum calculated tensile stress. Distributed loading angles greater than 30° show a significant (>10%) deviation from point loading ($2\alpha = 0$) conditions.

## 3. Finite element simulation method

Two-dimensional finite element (FEM) simulations were conducted using the commercial software ABAQUS Version 6.1 (HKS Inc., Pawtucket, RI). Static stress analysis was performed with a geometric model (Fig. 4) that consisted of 2700 continuum, plane stress or plane strain, 4-noded full integration elements. Due to symmetry, only a quarter of the entire geometry was modeled. Uniaxial loading was performed by imposing a vertical displacement, $U$, of up to 10% of the initial diameter, $D$, using a rigid surface which interacts with the finite element mesh via a frictionless or frictional contact. Included in Figs 2c and 4 is a representation of the contact-flattening event.

Three types of materials were used in the simulations: (i) linear elastic which is useful for brittle materials, (ii) linear elastic, perfectly plastic (Mises yield surface), in order to incorporate the effects of limited ductility and (c) linear elastic, perfectly plastic porous using Gurson's model, which is capable of describing porous materials with low levels of porosity [34]. Table I depicts the parameters used in this FEM work. The following parametric studies were covered: (i) elastic properties, (ii) contact friction, (iii) plane stress ($\sigma_z = 0$) or plane strain ($\varepsilon_z = 0$) conditions, (iv) yield strength and (v) relative density at various levels of yield strength. Some of the material properties chosen are based on published results [27, 28, 35] of microcrystalline cellulose.

## 4. Finite element simulation results

### 4.1. Elastic simulations

Figs 5 and 6 show a typical distribution of Mises, hydrostatic and maximum principal tensile stress normalized with respect to the elastic modulus, respectively, resulting from the elastic simulation. Mises stress is the stress invariant that represents the distortional intensity of the stress-state, while hydrostatic stress is the stress invariant that is responsible for volume changes [36]. The maximum of Mises stress occurs just under the

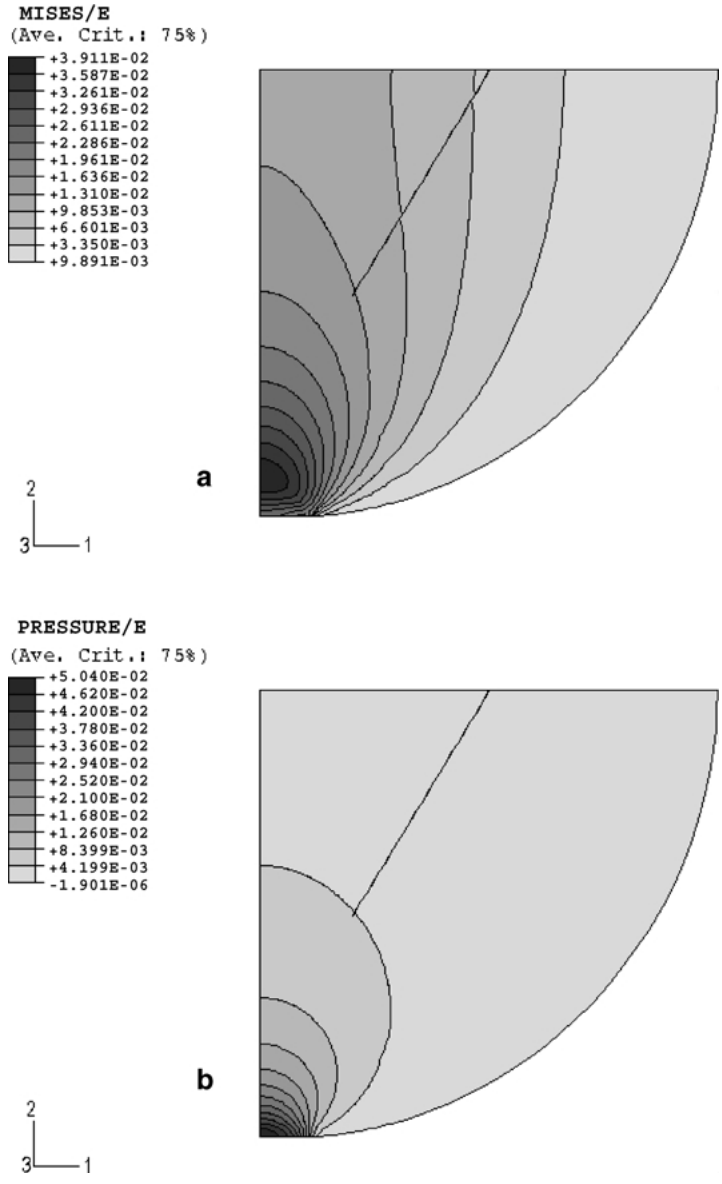


*Figure 5* Contour of (a) Mises stress and (b) hydrostatic stress from simulation using parameters from #1 (Table I) at $U/D = 0.02$ and $\delta/D = 0.115$ normalized for elastic modulus.

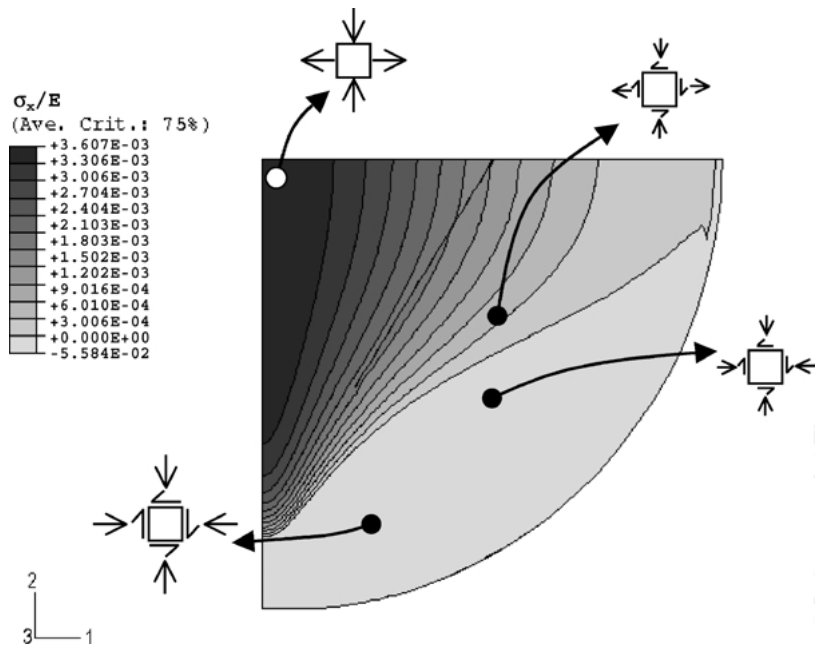


*Figure 6* Contour of $\sigma_x$ stress normalized for elastic modulus from simulation using parameters from #1 (Table I) at $U/D = 0.02$ and $\delta/D = 0.115$. Only tensile stresses are plotted.

surface, as shown previously [37], and is a direct effect of the generated contact stresses. In addition, the maximum hydrostatic pressure occurs at this contact, which may lead to local densification of the specimen.

The simulations show that maximum principal tensile stresses develop in the transverse direction to loading with a maximum at the center as predicted by the Hertz and Hondros solutions. Such stress is statistically responsible for brittle fracture of an elastic material (Fig. 6). This distribution of tensile stresses also explains the orientation of failure along the loaded axis observed experimentally. The contour of transverse tensile stress matches those seen in previous experimental [3, 10, 18, 21, 38–40] or theoretical/numerical work [4, 7, 16, 21, 29–33]. Fig. 7 shows that the stresses from the linear elastic simulation(s) (e.g., simulation #1, Table I) are in agreement with the Hertz solution (Equation 1) near the center of the specimen along the $x$ (Fig. 7a) and $y$ (Fig. 7b) axis. Disagreement is found to occur near the rigid boundary contact ($x/R$ or $y/R = 1$) where the analytical solutions are not valid.

For all linear elastic simulations (#1–5, Table I), the stress field scales with the external load and is independent of the elastic properties. A small region of tensile stress is generated near the rigid contact. At this level of boundary displacement ($U/D = 2\%$), the tensile stress at the edge of the contact is less than 5% of the maximum tensile stress seen along the vertical diameter. Regardless of this difference in magnitude, principal tensile stresses generated in this region may give rise to occasional failure due to favorably oriented surface cracks.

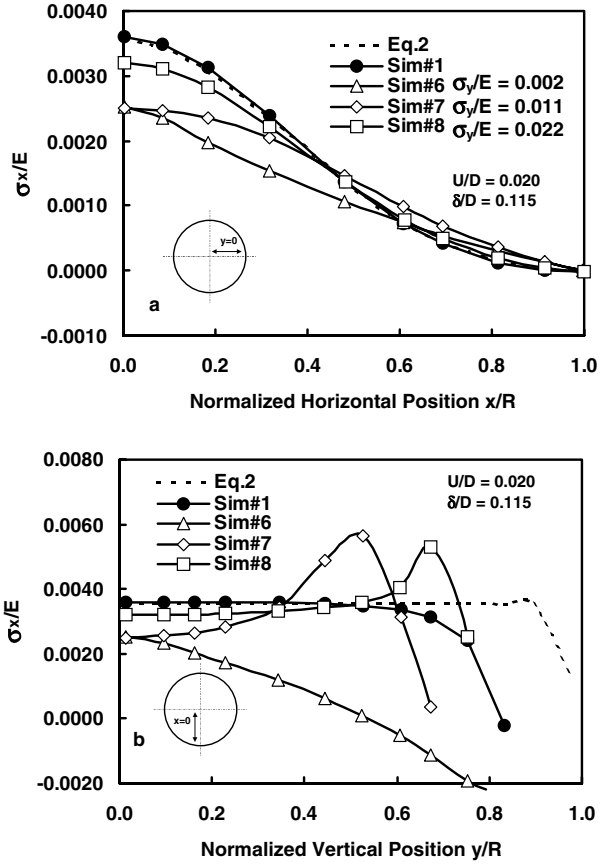


*Figure 7* Transverse stresses ($\sigma_x$) normalized for elastic modulus generated from elastic #1 (Table I) and elasto-plastic finite element simulations #6–8 (Table I) as compared to the Hertz solution (Equation 1) along (a) horizontal diameter ($y = 0$); where $x/R = 1$ is at the compact edge and (b) the vertical diameter ($x = 0$); where $y/R = 1$ is at the compact edge.

## 4.2. Elasto-plastic simulations

The incorporation of plasticity (e.g. simulations #6–8, Table I) into the finite element model, leads to substantial deviation between the analytical elastic expressions and the numerical elastoplastic solution along both the $x$ (Fig. 7a) and $y$-axis (Fig. 7b). This difference depends upon the magnitude of the yield stress to elastic modulus ratio. For a given relative displacement, $U/D$, between the platens, as the material yield strength increases the deviation from the analytical solution decreases near the geometric center.

In addition, several aspects of the stress-state change within the specimen with the incorporation of plasticity (e.g., simulations #6–8, Table I) into the finite element model. First, although the maximum principal stress is still in the transverse direction, the location of this stress shifts away from the center e.g., Fig. 8a (Simulation 7, Table I) demonstrates this off-center maximum principal stress at 2% diametrical strain. The magnitude of this maximum principal tensile stress is approximately 2.5–3 times the level predicted by the elastic solution (Equation 4). Plastic deformation initiates under the contact with the rigid platens (region of highest Mises stress, Fig. 8b) and expands towards the center as the overall deformation progresses. The maximum principal stress occurs at the boundary of the plastically deformed region and shifts as the edge of the plastically deforming region expands towards the center (Fig. 9). Eventually, when the plastic deformation spreads through the whole specimen, the location of the maximum principal stress returns to the center. The exact position and magnitude of the maximum tensile stress is a function of the ratio of elastic to plastic material properties as well as rigid platen displacement (Fig. 9). A similar off-center peak, occurring near $y/R = 0.4$, was noticed in the experimental work of Pitt *et al.* using photoelasticity on the diametrical compression test with convex cylindrical disks [21]. In that work, an epoxy resin Araldite CT200 (Ciba-Geigy Ltd.) cured with 30% w/w Hardener 901 was used, which has a published elastic modulus and yield stress of 3 GPa and 170 MPa, respectively.

The volume over which all of the maximum transverse stress is acting shows a significant reduction in comparison with the purely elastic simulations. This has implications, on the statistics of defect size, location, and orientation as they relate to compact failure [2–4, 6, 10].

Similar to the elastic case, tensile principal stresses also develop at the edge of the specimen near the region of platen contact. Their magnitude reaches almost 50% of the maximum tensile stress in the specimen (enlarged area of Fig. 8), however, occurs over a small material volume. In combination with the higher sensitivity of surface cracks, such tensile stresses can account for occasional failures observed experimentally to initiate at this location [9, 10, 17, 38, 39].

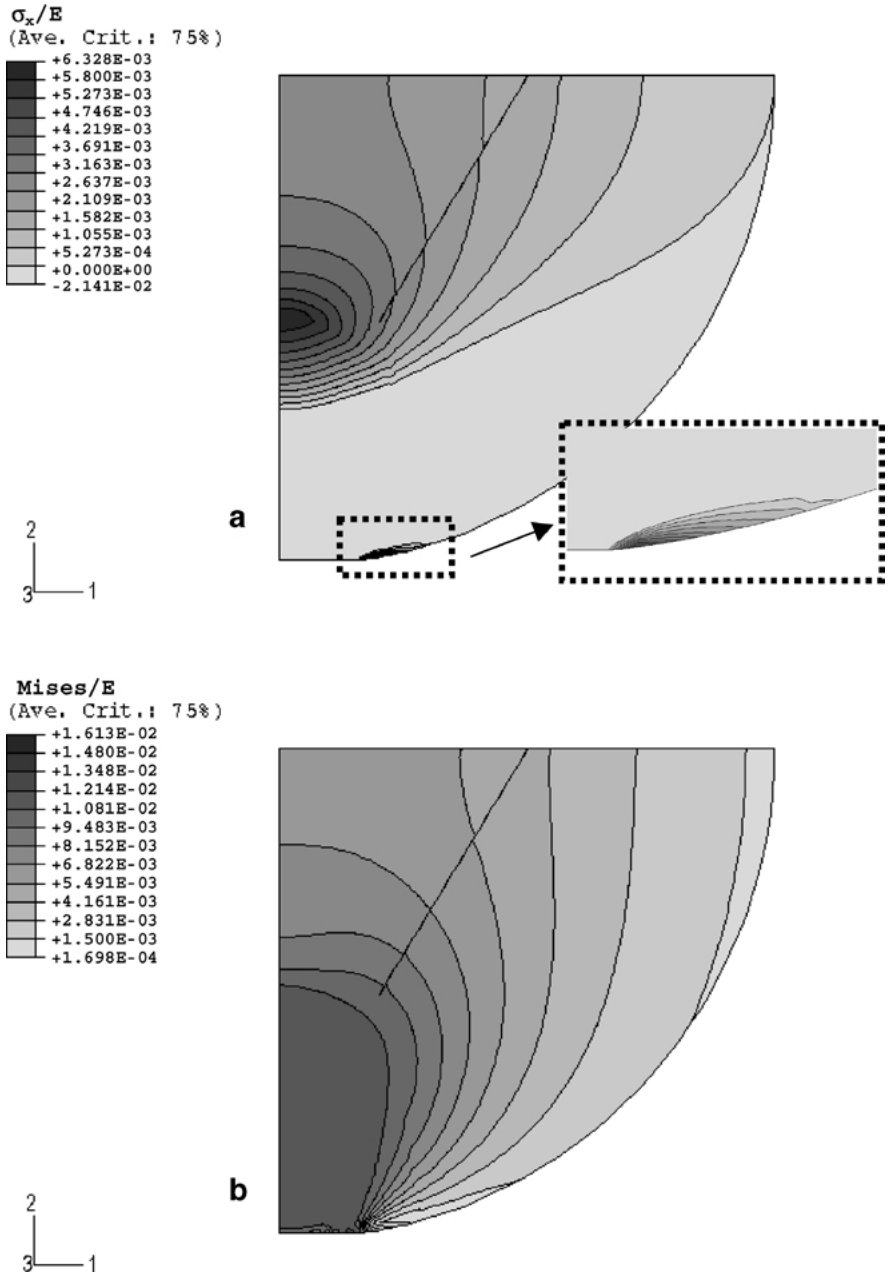


*Figure 8* Contour of (a) $\sigma_x$ and (b) Mises stress normalized for elastic modulus from simulation using parameters from #7 (Table I) at $U/D = 0.02$ and $\delta/D = 0.115$. Only tensile stresses are plotted in the $\sigma_x$ contour. [Note that a maximum of 0.011 should appear on the graph – any larger numbers are interpolation error].

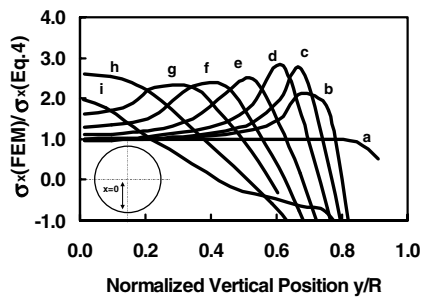


*Figure 9* Normalized stress profiles for elastoplastic simulation (#7, Table I) as a function of position along the vertical diameter ($y/R = 1$ is the compact edge) and diametrical strain ($U/D$): (a) 0.2%; (b) 1.1%; (c) 1.3%; (d) 1.6%; (e) 2.0%; (f) 2.5%; (g) 3.0%; (h) 5.0%; (i) 10.0%.

### 4.3. Porous elasto-plastic simulations

Powder compacts are usually not fully dense, and therefore the volume of pores and their subsequent densification may play a role in the local stress field. This densification event was simulated using the Gurson porous plasticity model [34] (Simulations #26–33, Table I) for initial relative densities of 0.80 and 0.90 as well as different modulus to yield strength ratios. The void fraction at a diametrical strain ($U/D$) of 0.02 is plotted as a contour in Fig. 10a. A region of high density is observed near the rigid boundary contact near the region of highest hydrostatic pressure, Fig. 10d. Similar to the elastoplastic simulations, an off-center maximum principal tensile stress of 2.5–3.0 times the elastic simulation was seen for these simulations as well Fig. 10b.

## 5. Experimental verification

To corroborate the simulations presented above, experiments were conducted for two model materials:

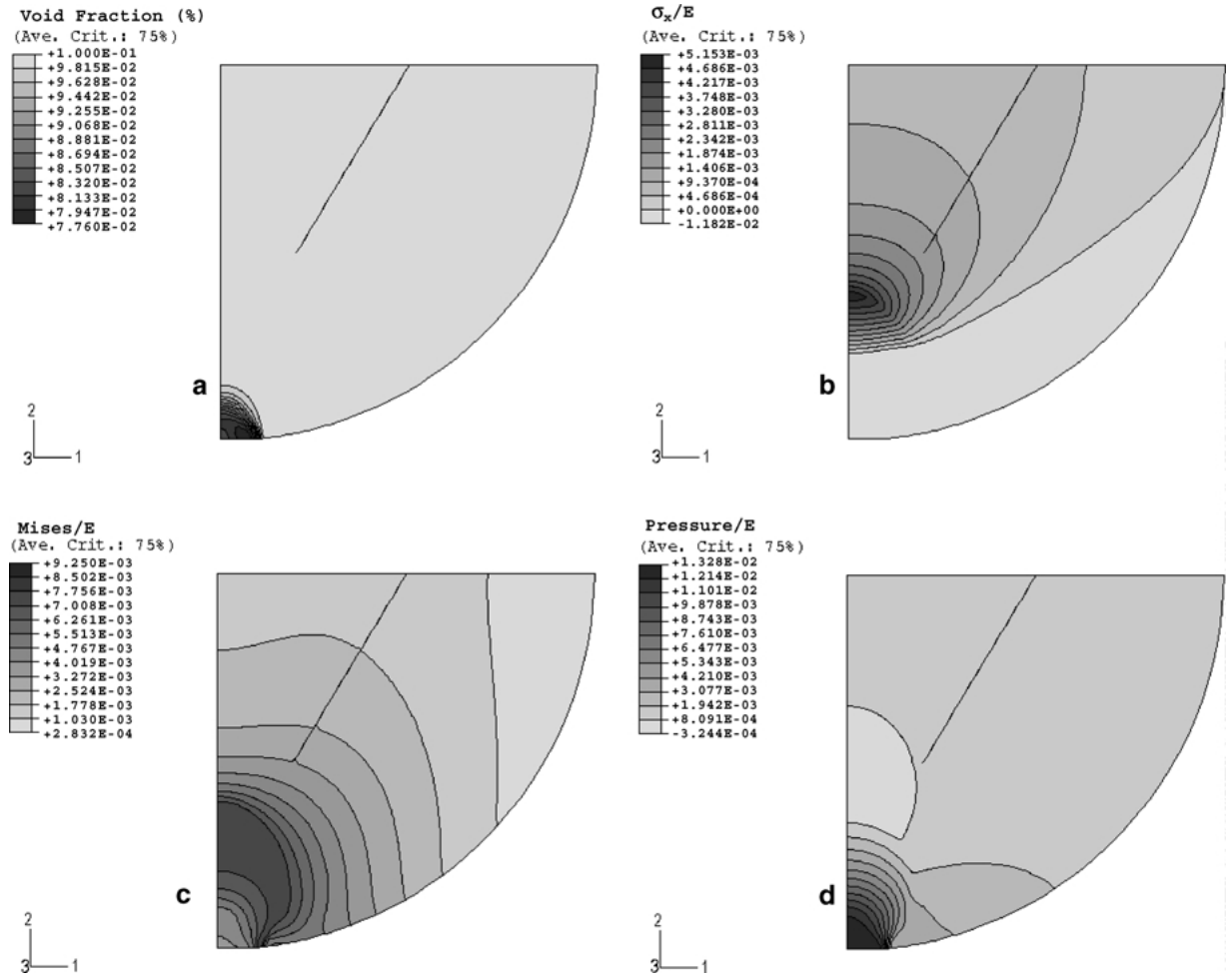


*Figure 10* Contour of (a) void fraction using a porous plasticity model for initial relative density of 0.90 and $\sigma_{\text{yield}}/E = 0.010$ at $U/D = 0.02$ (b) $\sigma_x$ (c) Mises and (d) hydrostatic (pressure) stress normalized for elastic modulus from simulation using parameters from #24 (Table I). Only tensile stresses are plotted in the $\sigma_x$ contour.

elastic—dicalcium phosphate anhydrous (DCP), a brittle ceramic and elastoplastic—microcrystalline cellulose (MCC), a soft deformable natural macromolecule. Disk specimens of 10.32 mm in diameter were compressed on an automated Carver Press (Carver, Inc., Wabash, IN) to a measured relative density of 0.8. An electromechanical material testing system (MTS Alliance RT50, MTS Systems Corporation, Eden Prairie, MN) was used to conduct diametrical compression. In this experiment, a 5-kN load cell was used to perform diametrical compression at a displacement rate of 4 mm/min on the above compacts between 101.6 mm hardened steel platens (HRC > 58). Typical failed compacts are shown in Fig. 11. The major measured parameters were the load to failure ($P_f$), the strain to failure ($U_f/D$) as well as the length of the flattened contact ($\delta/D$), which are schematically represented in Fig. 2c. Force and displacement were recorded for the calculation of stress (Equation 4) and strain ($U/D$) as shown in Fig. 12. In this plot, the difference in material properties between DCP and MCC is readily apparent. The "brittle" DCP exhibits linear elastic behavior with an

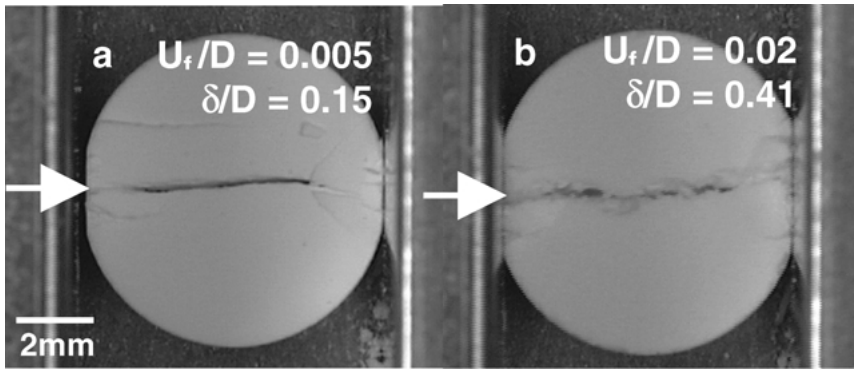


*Figure 11* Optical images of fractured, by diametrical compression, 10.32 mm flat faced compacts of (a) dicalcium phosphate anhydrous with a RD of 0.80 and (b) microcrystalline cellulose with a RD of 0.83.

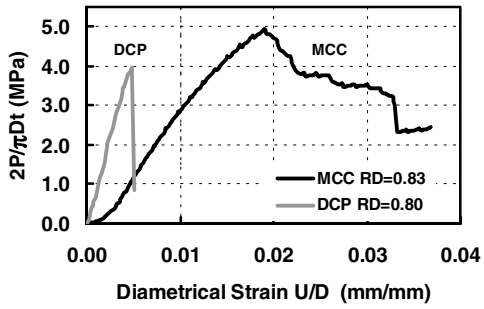


*Figure 12* Stress-strain data for 10.32 mm flat faced compacts undergoing diametrical compression at 4 mm/min for dicalcium phosphate anhydrous (DCP; Relative Density = 0.80) and microcrystalline cellulose (MCC; Relative Density = 0.83).

abrupt failure at a stress of 4 MPa and a strain of 0.005. The behavior of the "plastic" MCC is quite different. Significant diametrical strain of nearly 0.02 is induced before initial failure proceeds at a stress of 5 MPa. The fracture in this case is more gradual, and the material is able to absorb more energy as it fails.

Of particular interest is the exact location of crack initiation and propagation for materials that deform permanently. In other words, whether a simulated off-center maximum principal tensile stress (Fig. 8) leads to an off-center crack initiation. To illustrate this, high speed images were captured (Fig. 13) at 500 frames/s (Redlake Motionscope 1000S-110S-0001, Morgan Hill, CA) during a diametrical compression test of MCC using the MTS Alliance RT50. Image analysis (Image-Pro Plus v4.5, Media Cybernetics, Silver Spring, MD) was performed on these images near the moving platen, at the compact center, and near the static platen (Fig. 14). Drastic changes in pixel intensity are interpreted as cracks, and are marked with a circle in the figure. Careful observation shows that the crack originates along the loading direction near the loading platen after about 12 ms, a second crack initiates near the static platen after 22 ms, and both cracks propagate towards the center to form a continuous diametrical crack at 28 ms. Several research groups used various techniques to produce similar results on inhomogeneous and off-center crack initiation and propagation for materials that show both elasticity and plasticity [9, 10, 17, 38, 39].

## 6. Discussion

The finite element solution of elastic diametrical compression shows that the Hertz solution accurately predicts the magnitude and location of the maximum principal stress (Figs 6 and 7) as was also shown before [4, 7, 16, 21, 30–33] as well as with work conducted previously using experimental techniques such as photoelasticity [3, 10, 18, 21, 38, 40]. At a level of diametrical strain of 2%, for all elastic parameters investigated (Table I), only a $\pm 0.6\%$ deviation is realized (Fig. 15b). In general, the failure of brittle materials occurs at relatively low levels of strain (less than 2%), which deems the equation for tensile strength (Equation 4) valid. In fact, the intention of the diametrical compression test is to replace the tedious sample preparation used for tensile testing of complex shaped specimens of brittle

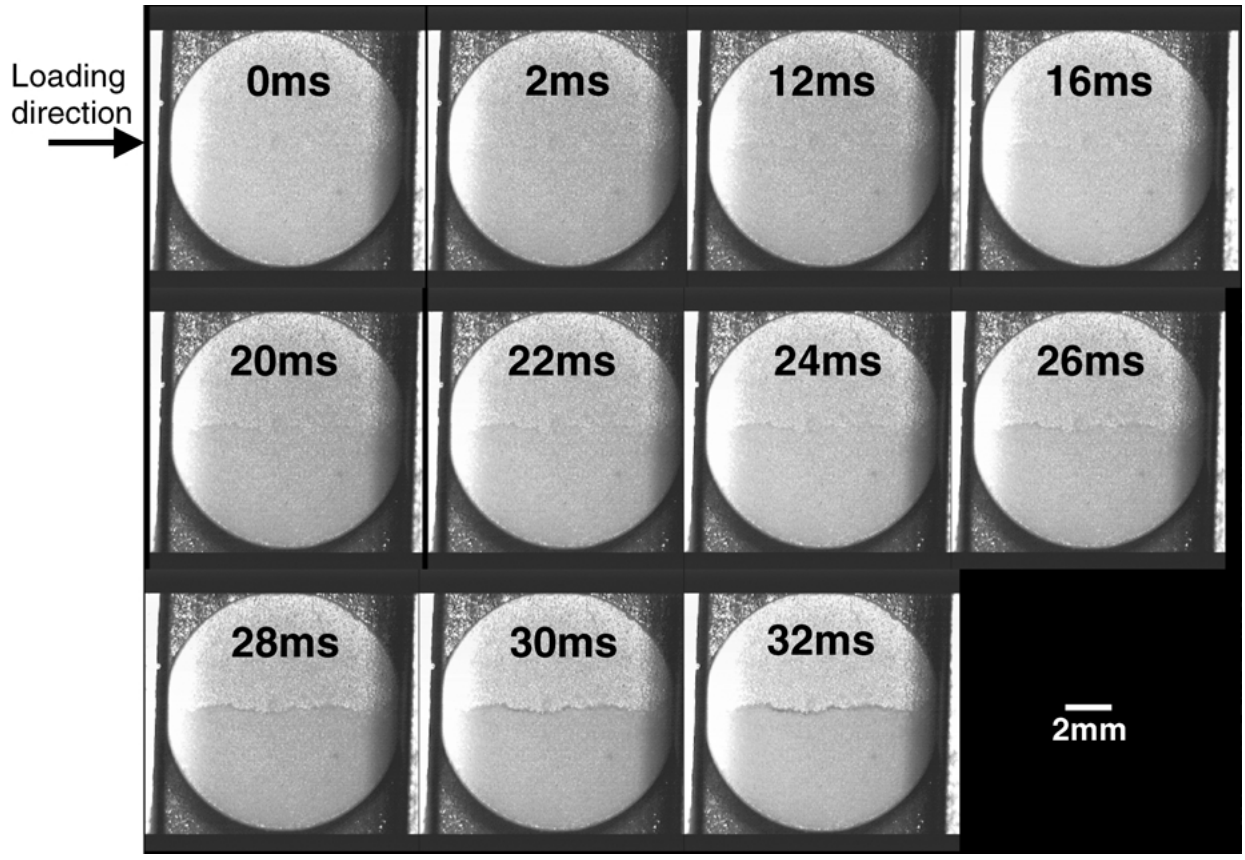


*Figure 13* Time elapsed optical images of the diametrical compression test for a 10.32 mm flat faced microcrystalline cellulose compact with a relative density of 0.83. Images captured with a high speed camera at 500 frames/second.

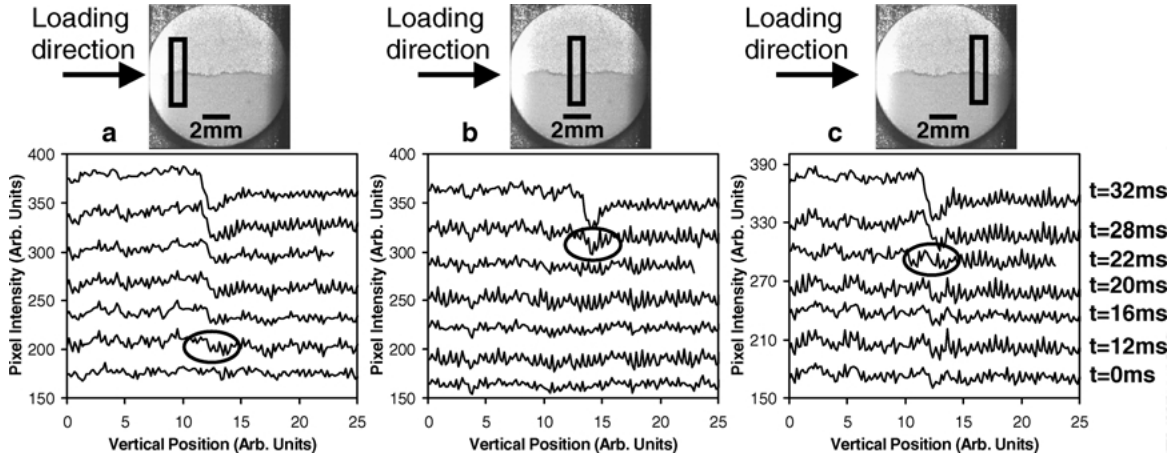


*Figure 14* Graphical representation, through image analysis of selected regions (black box), of crack initiation (circled area of graphs) and propagation as a function of time and position: (A) left edge of compact; (B) middle of compact; and (C) right edge of compact.

materials [1] and replace it with a simple and efficient test to determine tensile strength under a compressive mode of applied stress [8].

The validity of Equation 4 comes into question in the presence of plastic deformation, due to the severe effect on non-uniform stress distribution (Fig. 8) and off-center peak stress generation, which becomes a function of both diametrical strain (Fig. 9) and material properties (Fig. 15). The off-center peak of maximum tensile stress is much higher, in some cases three times greater, than the Hertz estimate (Equation 4). Under these circumstances, the peak force used to calculate strength according to Equation 4 underestimates the tensile strength. The maximum principal stress has a local peak compared to the elastic solution where the maximum transverse stress is practically uniform along the axial direction. This difference has significant implications on the statistics of fracture, given the importance of the volume arguments in specimen failure. Moreover, significant tensile stresses develop at the edge of the contact (Fig. 8), which can lead to a different mode of fracture compared to the purely elastic deforming bodies.

Plastic deformation appears at relatively large diametrical strains. In other words, the strain at which failure occurs becomes an important criterion for the validity of the Hertzian equation (Equation 4), under the assumptions of both homogeneous and inhomogeneous defect microstructure for materials with drastically different properties. To summarize the above results, a "validity map" of the Hertz solution was sketched on the basis of material property ratios ($\sigma_{\text{yield}}/E$), rigid boundary displacement, and results of the finite element simulations (#9–25, Table I). In Fig. 16 we plot the diametrical strain ($U/D$) at which a 10% deviation from the Hertzian solution (Equation 4) occurs. Above the plotted data, the Hertzian solution is considered invalid (>10% deviation) and below these data the Hertzian conditions are

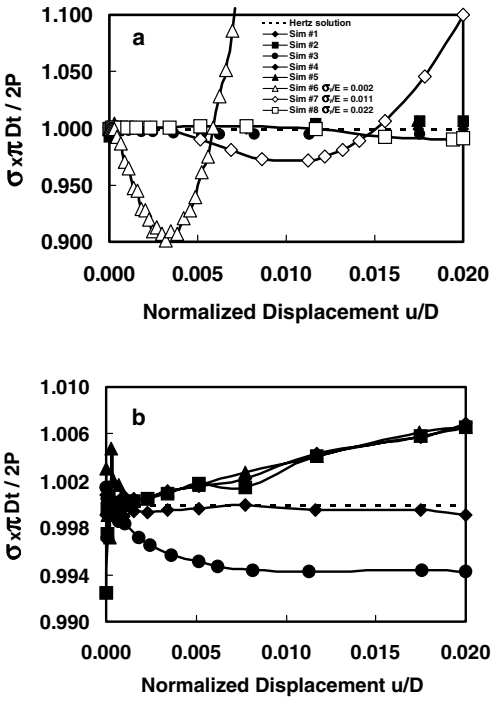


*Figure 15* Comparison between normalized Hertz solution (Equation 4) and (a) elastic #1–5 and elasto-plastic finite element simulations #6–8 and (b) elastic only simulations #1–5 as a function of rigid boundary displacement ($U$). Note differences in ordinate magnitude.

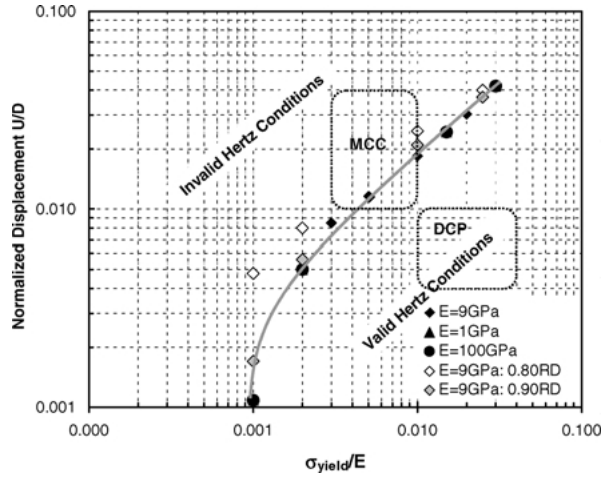


*Figure 16* Finite element simulation results (#9–22, Table I) representing the validity (within 10%) of the Hertzian equation for maximum tensile stress (Equation 4) as a function of material properties ($E$ and $\sigma_{\text{yield}}$) and normalized rigid boundary displacement ($U/D$). Shaded areas represent realistic ranges of properties and failure strains of microcrystalline cellulose (MCC) and dicalcium phosphate (DCP).

applicable, i.e. Equation 4 is a valid representation of the maximum principal stress-state. This trend appears to be a weak function of elastic modulus. However, as the yield strength to elastic modulus ratio decreases, the displacement (or flattened contact width) at which a deviation from Equation 4 occurs becomes very small. In terms of the porous plasticity simulations (#26–33, Table I), the "validity window" of Fig. 16 is increased with increasing porosity in the range investigated here.

As was seen in Fig. 10a, there is a region under the platen where the material densifies. This local change of material properties alters the way stresses are transferred into the center of the specimen, and is responsible for the smaller deviation from the predictions of Equation 4, for the conditions investigated here. The data presented here clearly show the dependence of material properties, relative density, and failure strain on the validity of the Hertzian and Hondros equations on accurately predicting the maximum transverse stress in a diametrically loaded body.

Ultimately, product development using strength as a criterion usually means cross comparison of data and thus data interpretation. Careful consideration should be given to the interpretation of diametrical strength data knowing that the materials used do deform plastically to some finite level and fall outside small composition/structure variations or a relatively narrow processing parameter window.

## 7. Conclusions

Finite element simulations of the diametrical compression test involving two-dimensional elements were completed for linear elastic, elasto-plastic, and porous elasto-plastic materials. Linear elastic finite element simulations show excellent agreement with previous work and analytical expressions. The effect of contact flattening has been demonstrated to have significance, for materials that show plastic deformation or densification, on the distribution and volume of transverse (tensile) stress. For plastically deforming materials, a better understanding of the internal stress-state has been demonstrated. The maximum transverse stress is located away from the compact center along the vertical diameter, which leads to a deviation from the Hertzian prediction of stresses in this region. If maximum principal stress is used as a fracture criterion, then the off-center peak will translate to off-center crack propagation, which was verified using high-speed photography and image analysis. The non-homogenous stress distribution under diametrical compression for plastically deforming materials is also a function of the ratio of elastic to plastic material properties as well as diametrical strain. The finite element simulations also predict a significant amount of tensile stress generated near the loading boundary, which is realized in crack formation near this area. Simulations that involve compacts of different initial relative density show significant densification near the region of platen contact under diametrical loading.

The Hertzian equation generally used to calculate tensile strength, $\sigma_f = 2P/\pi Dt$, is shown to be suitable for materials which undergo brittle fracture (linear elastic). Careful attention to both the location of crack propagation and diametrical strain at which failure occurs should be made when calculating tensile strength for materials which deform plastically and suffer from substantial irreversible contact flattening. A validity map of the Hertzian equation used to estimate tensile strength has been clearly demonstrated based on finite element simulations for a range of elastic and inelastic material properties.


## Acknowledgment

Support for this work was provided by the NSF-GOALI project CMS-0100063.


## References


1. ASTM Designation E 8-01, "Standard Test Method for Tension Testing of Metallic Materials" (Philadelphia, 2001).
2. P. STANLEY and J. M. NEWTON, *J. Powder Bulk Sol. Technol.* **1** (1977) 13.
3. P. STANLEY, *Int. J. Pharm.* **227** (2001) 27.
4. L. J. NEERGAARD, D. A. NEERGAARD and M. S. NEERGAARD, *J. Mater. Sci.* **32** (1997) 2529.
5. A. BRÜCKNER-FOIT, T. FETT, D. MUNZ and K. SCHIRMER, *J. Euro. Ceram. Soc.* **17** (1997) 689.
6. W. WEIBULL, *J. Appl. Mech.* **18** (1951) 293.
7. G. HONDROS, *Aust. J. Appl. Sci.* **10** (1959) 243.
8. ASTM Designation D 3967-95a, "Standard Test Method for Splitting Tensile Strength of Intact Rock Core Specimens" (Philadelphia, 1996).
9. J. F. LABUZ, S. CATTANEO and L. H. CHEN, *Const. Bldg. Mat.* **15** (2001) 225.
10. G. BERNAUER, U. SOLTÉSZ, and R. SCHÄFER, *Adv. Sci. Technol.* **3B** (1995) 1105.
11. R. H. MARION and J. K. JOHNSTONE, *Amer. Ceram. Soc. Bull.* **56**(11) (1977) 998.
12. D. K. SHETTY, A. R. ROSENFIELD and W. H. DUCKWORTH, *J. Amer. Ceram. Soc.* **69**(6) (1986) 437.
13. G. DEWITH, *J. Mater. Sci. Let.* **3** (1984) 1000.
14. O. COUBE, PhD Thesis, U. Pierre et Marie Curie, Paris VI, 1999.
15. F. BONOLLO, B. MOLINAS, I. TANGERINI and A. ZAMBON, *Mater. Sci. Tech.* **10** (1994) 558.
16. L. EHRNFORD, *Acta Odontologica Scandinavica* **39**(1) (1981) 55.
17. L. EHRNFORD, *ibid.* **39**(2) (1981) 71.
18. E. P. LAUTENSCHLAGER and J. K. HARCOURT, *J. Dental Research*, **49**(1) (1970) 175.
19. J. T. FELL and J. M. NEWTON, *J. Pharm. Sci.* **59**(5) (1970) 688.
20. K. G. PITT, J. M. NEWTON and P. STANLEY, *J. Mater. Sci.* **23** (1988) 2723.
21. *Idem., J. Phys. D: Appl. Phys.* **22** (1989) 1114.
22. E. N. HIESTAND AND C. B. PEOT, *Pharm. Tech.* **63** (1974) 605.
23. H. G. KRISTENSEN, P. HOLM and T. SCHAEFER, *Powder Technol.* **44** (1985) 227.
24. T. L. ANDERSON, "Fracture Mechanics: Fundamentals and Applications," (CRC Press, Boca Raton, FL, 1995).
25. C. NYSTROM, W. ALEX and K. MALMQVIST, *Acta Pharm. Suec.* **14** (1977) 317.
26. K. SHINOHARA, C. E. CAPES and A. E. FOUDA, *Powder Technol.* **32** (1982) 163.
27. R. J. ROBERTS and R. C. ROWE, *Int. J. Pharm.* **37** (1987) 15.
28. G. ALDERBORN and C. NYSTRÖM, "Pharmaceutical Powder Compaction Technology" (Marcel Dekker, 1996).

29. H. HERTZ, Gesammelte Werke (Collected Works), Leipzig, 1895.
30. D. MAUGIS, "Contact, Adhesion and Rupture of Elastic Solids" (Springer Series in Solid-State Sciences, 2000) Vol. 130.
31. S. P. TIMOSHENKO and J. N. GOODIER, "Theory of Elasticity" (McGraw-Hill, New York, 1970).
32. M. K. FAHAD, *J. Mat. Sci.* **31** (1996) 3723.
33. K. SHINOHARA and C. E. CAPES, *Powder Technol.* **24** (1979) 179.
34. C. S. DESAI and H. J. SIRINARDANE, "Constitutive Laws for Engineering Materials" (Prentice-Hall, Inc., Englewood Cliffs, NJ, 1984).
35. R. J. ROBERTS, R. C. ROWE and P. YORK, *Int. J. Pharm.* **105** (1994) 177.
36. G. E. DIETER, "Mechanical Metallurgy" (McGraw-Hill, London, UK, 1988).
37. S. BIWA and B. STORAKERS, *J. Mech. Phys. Solids* **43**(8) (1995) 1303.
38. A. CASTRO-MONTERO, Z. JIA and S. P. SHAH, *ACI Mat. Journal* **92/M29** (1995) 268.
39. C. A. TANG, X. H. XU, S. Q. KOU, P. A. LINDQVIST and H. Y. LIU, *Int. J. Rock Mech. & Min. Sci.* (In press).
40. Y. HIRAMATSU and Y. OKA, *ibid.* **3** (1966) 89.

*Received 15 July 2002*
*and accepted 9 June 2003*